Advanced 3D Monte Carlo Algorithms for Biophotonic and Medical Applications

Lewis McMillan

University of
St Andrews

This thesis is submitted in partial fulfilment for the degree of
PhD
at the
University of St Andrews

March 2019

Declaration

I, Lewis McMillan, hereby certify that this thesis, which is approximately ***** words in length, has been written by me, that it is the record of work carried out by me, or principally by myself in collaboration with others as acknowledged, and that it has not been submitted in any previous application for a higher degree.

I was admitted as a research student in September 2015 and as a candidate for the degree of PhD in September 2015; the higher study for which this is a record was carried out in the University of St Andrews between 2015 and 2019.

Date.......................... Signature of candidate ....

I hereby certify that the candidate has fulfilled the conditions of the Resolution and Regulations appropriate for the degree of PhD in the University of St Andrews and that the candidate is qualified to submit this thesis in application for that degree.

Date .... Signature of supervisor ....

Date .... Signature of supervisor ....

Abstract

Lorem ipsum dolor sit amet, consectetuer adipiscing elit. Ut purus elit, vestibulum ut, placerat ac, adipiscing vitae, felis. Curabitur dictum gravida mauris. Nam arcu libero, nonummy eget, consectetuer id, vulputate a, magna. Donec vehicula augue eu neque. Pellentesque habitant morbi tristique senectus et netus et malesuada fames ac turpis egestas. Mauris ut leo. Cras viverra metus rhoncus sem. Nulla et lectus vestibulum urna fringilla ultrices. Phasellus eu tellus sit amet tortor gravida placerat. Integer sapien est, iaculis in, pretium quis, viverra ac, nunc. Praesent eget sem vel leo ultrices bibendum. Aenean faucibus. Morbi dolor nulla, malesuada eu, pulvinar at, mollis ac, nulla. Curabitur auctor semper nulla. Donec varius orci eget risus. Duis nibh mi, congue eu, accumsan eleifend, sagittis quis, diam. Duis eget orci sit amet orci dignissim rutrum.

Nam dui ligula, fringilla a, euismod sodales, sollicitudin vel, wisi. Morbi auctor lorem non justo. Nam lacus libero, pretium at, lobortis vitae, ultricies et, tellus. Donec aliquet, tortor sed accumsan bibendum, erat ligula aliquet magna, vitae ornare odio metus a mi. Morbi ac orci et nisl hendrerit mollis. Suspendisse ut massa. Cras nec ante. Pellentesque a nulla. Cum sociis natoque penatibus et magnis dis parturient montes, nascetur ridiculus mus. Aliquam tincidunt urna. Nulla ullamcorper vestibulum turpis. Pellentesque cursus luctus mauris.

Acknowledgements

Lorem ipsum dolor sit amet, consectetuer adipiscing elit. Ut purus elit, vestibulum ut, placerat ac, adipiscing vitae, felis. Curabitur dictum gravida mauris. Nam arcu libero, nonummy eget, consectetuer id, vulputate a, magna. Donec vehicula augue eu neque. Pellentesque habitant morbi tristique senectus et netus et malesuada fames ac turpis egestas. Mauris ut leo. Cras viverra metus rhoncus sem. Nulla et lectus vestibulum urna fringilla ultrices. Phasellus eu tellus sit amet tortor gravida placerat. Integer sapien est, iaculis in, pretium quis, viverra ac, nunc. Praesent eget sem vel leo ultrices bibendum. Aenean faucibus. Morbi dolor nulla, malesuada eu, pulvinar at, mollis ac, nulla. Curabitur auctor semper nulla. Donec varius orci eget risus. Duis nibh mi, congue eu, accumsan eleifend, sagittis quis, diam. Duis eget orci sit amet orci dignissim rutrum.

Nam dui ligula, fringilla a, euismod sodales, sollicitudin vel, wisi. Morbi auctor lorem non justo. Nam lacus libero, pretium at, lobortis vitae, ultricies et, tellus. Donec aliquet, tortor sed accumsan bibendum, erat ligula aliquet magna, vitae ornare odio metus a mi. Morbi ac orci et nisl hendrerit mollis. Suspendisse ut massa. Cras nec ante. Pellentesque a nulla. Cum sociis natoque penatibus et magnis dis parturient montes, nascetur ridiculus mus. Aliquam tincidunt urna. Nulla ullamcorper vestibulum turpis. Pellentesque cursus luctus mauris.

Contents

Abbreviations

BPM beam propagation method.

FDTD finite difference time domain.

HOBBs higher order Bessel beams.

MCRT Monte Carlo radiation transfer.

PSTD pseudo-spectral time-domain.

RTE radiative transfer equation.

List of Figures

Chapter 1

Quasi-wave/particle Monte Carlo Algorithm, φMC

1.1 Introduction

Complex shaped light beams have been used in a wide variety of applications in biophotonics and medicine. From using Airy beams to move particles and cells [1], Bessel beam "tractor beams" [2], using Airy and Bessel beams for better field of view in light-sheet microscopy [3], and using Laguerre-Gaussian beams to optical trap optically reflective particles [4].

However simulation techniques for modelling complex shaped beams in biological tissue is lacking. Currently there are a number of techniques that can model these beams in biological tissue, however they all have downsides. These methods include diffusion approximation to the radiative transfer equation (RTE), finite difference time domain (FDTD), pseudo-spectral time-domain (PSTD), beam propagation method (BPM), and Monte Carlo radiation transfer (MCRT).

As discussed in ??, the diffusion approximation has many downsides when it comes to modelling light propagation in biological tissue. FDTD involves using a finite difference method in order to solve Maxwell's equations. However this is computationally intensive and requires a grid resolution of $\sim \lambda/20$ and thus most models are restricted to 2D [5,6]. PSTD like the FDTD is also computationally intensive, though to a lesser extent [5]. BPM is a fairly computational efficient method of propagating light beams, compared to FDTD or PSTD. However, the BPM uses the slowly varying envelope approximation, which limits some of the problems it can be utilised for. BPM is also generally a uni-directional propagation method, though it can be adapted to model bidirectional propagation, this can lead to issues in the model's accuracy [5,7].

The final method, MCRT, in general cannot model complex beams where the wave like behaviour of photons is required to form, or propagate the beam. For example, traditional MCRT methods cannot model Gaussian beams, as Gaussian beams have a finite beam waist at their focus (see Fig. 1.6). MCRT (along with geometric optics) predicts that Gaussian beams have an infinitely small waist.

Various authors have tried to model complex beams that require wavelike behaviours using MCRT. Some of the techniques used by these authors include: artificial beam steering [8], generating skew rays [9], complex ray tracing [10], decomposition [11], electric field Monte Carlo [12], and wavefront tracing [13]. However all these techniques either inaccurately model Gaussian beams, are complex to implement, or computational intensive (more so than MCRT

usually is). There have been some attempts at using the techniques presented in this chapter, to modify MCRT algorithms into algorithms that can model diffraction and interference [14–18]. These authors have good results, but either do not detail their methods, do not attempt to treat scattering or are in the x-ray regime.

This chapter modifies the MCRT method, from a "ballistic" photon method into a quasi-ballistic/wave photon method so that the wave behaviour of photons can be modelled. This algorithm, φMC, allows the modelling of complex shaped beams such as Bessel beams and Gaussian beams, without much modification of the underlying MCRT code.

We present a through investigation of the method used to turn a ballistic regime MCRT method in to a quasi-wave/ballistic method. The method is validated against theoretical and experimental data for various different beam types including: Bessel (including higher orders), and Gaussian beams. Treatment of the propagation through scattering media is also discussed.

1.2 Theory

To convert a MCRT simulation to be able to model wave like behaviour of photons, we introduce two concepts: tracking the complex phase of packets and the Huygens-Fresnel principle. This section presents a description of the modifications to the traditional MCRT algorithm, along side the theoretical background to both the concepts.

1.2.1 Complex Phase Tracking

The first concept we add to the MCRT method is assigning a complex phase to each packet. The phase is given to a packet at the beginning of the simulation depending on the input field. The packet is also given an initial complex electric field of the form:

$$E_0 = \frac{1}{N} \sqrt{\frac{P}{A}} \tag{1.1}$$

Where N is the number of packets run in a simulation, P is the power of the incident beam, and A is the area of the beam. This initial electric field is needed to compare different beams as in Section 1.6, and to normalise for number of packets run.

The phase is then tracked as the packet moves through the medium, over a distance l. Equation (1.2) shows how the phase is calculated.

$$\varphi = cos\left(\frac{2\pi l}{\lambda}\right) + i \; sin\left(\frac{2\pi l}{\lambda}\right) \tag{1.2}$$

Where φ [−] is the complex phase of a photon packet, l [m] is the distance the packet has travelled, λ [m] is the wavelength of the packet, and i is the solution to $x^2 = -1$. Now we can calculate the complex phase of a packet at a position P_o, if we know the distance it has travelled, and its original phase, see Fig. 1.1.

To model interference, we let the photon packets interfere with one another in a volume or area element. We do not model the interference at a point in space where photon packets cross, due to the ballistic nature of the MCRT simulation this does not occur with enough frequency in order to give a good signal to noise ratio. Therefore, interference takes place in a volume, dV, or area element, dA, instead. To calculate the interference from the phase, the phase is summed in each volume or area element and the absolute value taken, and then squared. Equation (1.3) shows the equation for interference for a volume element dV. A similar relation for calculating the interference on an area element dA also exists.

2
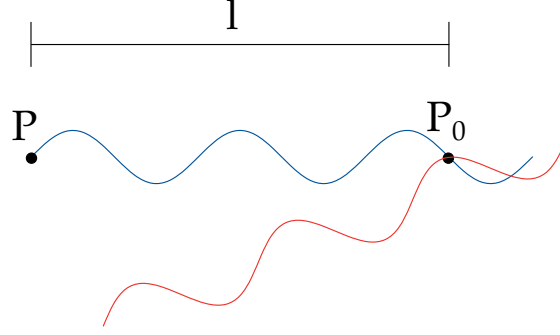
Figure 1.1: *Example of phase calculation when a photon has travelled a distance l. Figure also show an example of interference between two photons via addition of the complex amplitudes at the point P_0.*

$$I(\zeta) = \left| \sum_\zeta E_0 \, cos\left(\frac{2\pi l}{\lambda}\right) + i \sum_\zeta E_0 \, sin\left(\frac{2\pi l}{\lambda}\right) \right|^2, \quad \zeta = (x, y, z) \tag{1.3}$$

Where:

l is the total distance travelled by a photon $[m]$;

λ is the wavelength of the photon $[m]$;

I is the intensity at the ζth cell $[Wm^{-2}]$;

E_0 is the initial electric field of the packets as in Eq. (1.1) $[Vm^{-1}]$

and ζ is the xth, y^{th}, z^{th} cell, volume dV.

In addition to tracking the phase, the next principle needed to simulate the wave behaviour of light in MCRT is the Huygens-Fresnel principle.

1.2.2   Huygens-Fresnel Principle

The Huygens-Fresnel principle is a method that is used to help model the propagation of waves in the far field limit and the near field limit. The Huygens principle states [19–21]:

"Every point on a propagating wavefront serves as the source of spherical secondary wavelets, such as the source at some time later is the envelope of these wavelets."

The principle is illustrated in Fig. 1.2. Christiaan Huygens postulated this principle in 1678. The principle allowed Huygens to derive laws of refraction and reflection, but it failed to describe diffraction effects. This led to Augustin-Jean Fresnel in 1818, combining the Huygens principle with his own theory of interference [21, 22]. This principle, the Huygens-Fresnel principle, gave an accurate description of the propagation of light and diffraction effects. This was achieved by allowing the secondary wavelets to self interfere with one another, giving rise to an accurate description of the physical phenomena. Later, Gustav Kirchhoff gave a rigours mathematical description of the Huygens-Fresnel principle, which is the basis of diffraction theory [23, 24].

The Huygens-Fresnel principle allows the modelling of diffraction in both the near and far field. As the principle states that every point on the wavefront is a source of secondary spherical waves, this implies that there are "backward" waves. These "backward" waves are un-physical, and there is no experimental evidence of their existence. Thus Fresnel introduced an inclination factor to eliminate these "backward" waves. This inclination factor was later put on a rigorous

mathematical standing by Kirchoff, as it naturally fell out of his theory [23, 24]. Equation (1.4) shows the equation for the complex field at a point on a plane as derived by Kirchoff with the inclination factor.

$$u(\mathbf{r_1}) = \frac{1}{i\lambda} \int \int u(\mathbf{r_0}) \frac{\hat{\mathbf{s_0}} \cdot (\mathbf{r_1} - \mathbf{r_0})}{|\mathbf{r_1} - \mathbf{r_0}|^2} e^{ik|\mathbf{r_1} - \mathbf{r_0}|} dS_0 \tag{1.4}$$

Where:

u is the complex electric field $[Vm^{-1}]$;
λ is the wavelength $[m]$;
S_0 is a plane with surface normal $\hat{\mathbf{s_0}}$ [-];
k is the wavenumber $[m^{-1}]$;
and $\mathbf{r_n}$ are spatial coordinates [-].

The Huygens-Fresnel principle is implemented by sampling the light source on the surface of any lens or in a slit. In practise this means when for example, a plane wave is incident on a slit width a, and length b, the slit area is uniformly sampled for the initial position of the photon packets. The packets are then given a random direction, sampled towards the detector thus avoiding the non-existent "backward" waves. For the case of modelling propagation through a lens, the usual geometric optics approach is taken to propagate the packets through the lens. When the packet lies on the surface of the lens, the Huygens-Fresnel principle is invoked, and the packet is given a random direction (in the direction of the medium) and propagated as usual.

Our algorithm uses the Huygens-Fresnel principle and the tracking of complex phase to simulate diffraction effects, that would otherwise be absent from the simulation. The principle allows the algorithm to calculate the complex amplitude at a point, and thus the intensity at that point, essentially numerically simulating Eq. (1.4). These two concepts underpin the algorithm that allows various complex beams, and wave phenomena to be simulated within a ballistic method. The following sections validate the method against the theory and experimental data for propagation of various complex beams.
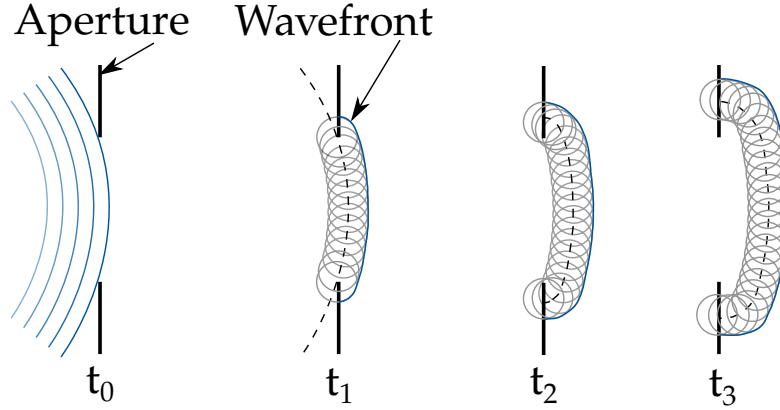
Figure 1.2: *Illustration of the Huygens-Fresnel principle. At t_0 a wave is incident on an aperture. Times t_1, t_2, and t_3 show the evolution of the wavefront using the Huygens-Fresnel principle. Dashed lines illustrate the wavefront position at the previous time step, and is the source of the Huygens-Fresnel wavelets.*

1.2.3 Validation of Phase Tracking Algorithm

Double Slit Experiment

The first test of our quasi-wave/particle MCRT algorithm*, φMC, is to compare our simulation to a double slit experiment. The double slit experiment, is a simple experiment where a monochromatic plane wave of light is incident on two slits distance apart d, and width b, and an interference pattern is observed on a screen a distance L away from the slits. The experiment is usually carried out with the detector screen in the far field, the so called Fraunhofer regime. The intensity pattern on the detector screen is as in Eq. (1.5):

$$I(x) \propto cos^2 \left(\frac{kdx}{2\sqrt{L^2 + x^2}} \right) sinc^2 \left(\frac{kax}{\sqrt{L^2 + x^2}} \right) \tag{1.5}$$

Where the *sinc* function is defined as $\frac{sin(x)}{x}$, for $x \neq 0$, k is the wavevector, $k = \frac{2\pi}{\lambda}$, and x is the horizontal position on the detector screen.

The simulation was carried out for a wavelength, λ, of 488 nm, a slit width of 10λ, slit separation of 80λ, and the detector screen positioned 10000λ away from the slits. Using the Huygens-Fresnel principle, each slit is a source of Huygens wavelets. The detector screen has dimensions, 1 mm^2 and there are 2051^2 bins, giving a bins an effective size: $\sim 488 \; nm$ or $\sim \lambda$. The initial position of the photon packets is sampled uniformly from the slit area, after randomly choosing one of the slits to emit from. A random direction is then chosen to ensure that the packets will hit the detector screen. The simulation was run with 10^9 packets, which took $\approx 10 \; mins$ to run on an 8 core Intel Xeon machine. This gave an accurate match to the theoretical expression, as seen in Fig. 1.3.
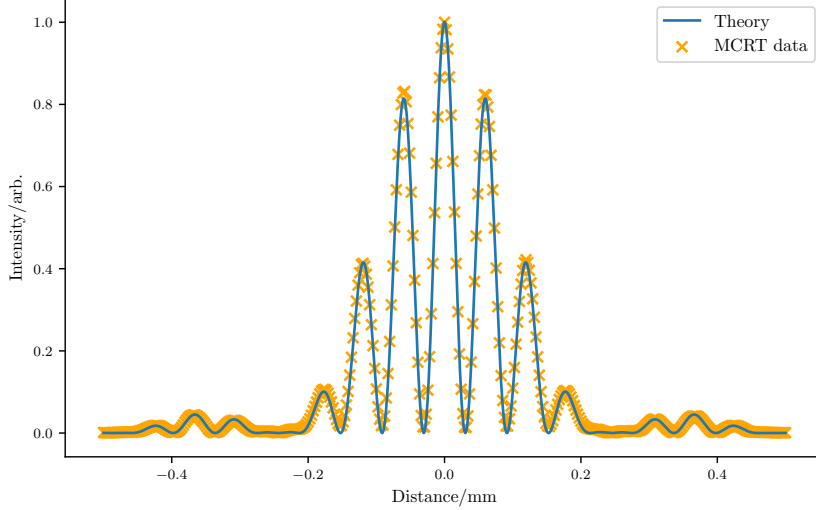
Figure 1.3: *Comparison of theory and simulation for the double slit experiment. For clarity only every 5th MCRT data point is plotted.*

---

*Though this example is not strictly MCRT, but rather ray tracing, as it involves no scattering. The full MCRT method will be used in later sections.

Diffraction by a Square Slit

φMC is also validated by simulating diffraction from a square aperture in the far and near field, the so call Fresnel and Fraunhofer regimes. Fresnel diffraction occurs in the near field when the *Fresnel number*, Eq. (1.6), is greater than 1.0. Fraunhofer diffraction occurs when the *Fresnel number* is less than 1.0.

$$F = l\sqrt{\frac{2}{\lambda r_0}} \tag{1.6}$$

Equation (1.6) is the Fresnel number, where l is the slit width, λ is the wavelength of the incident radiation, and r_0 is the distance from the aperture to the detector screen, as shown in Fig. 1.4.
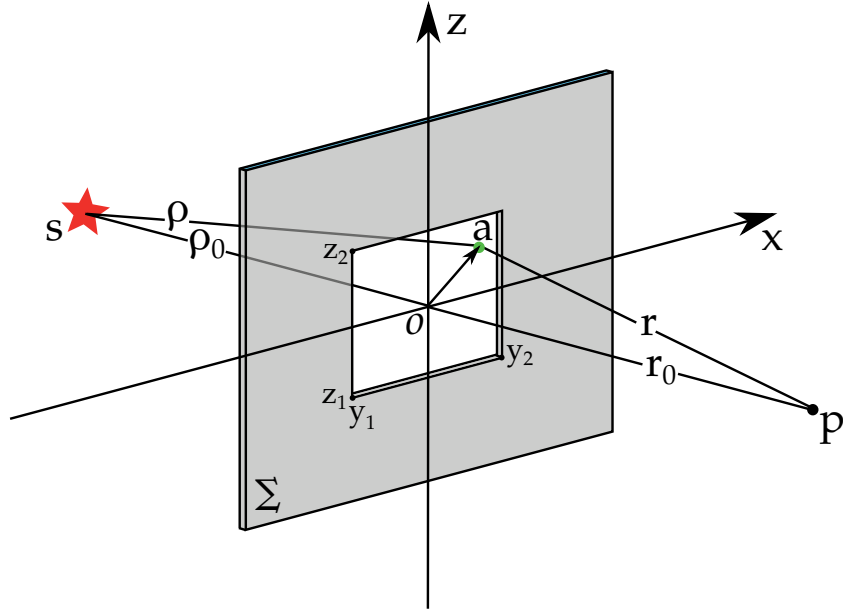
Figure 1.4: *Geometry of the square aperture used in the validation.*

To compare φMC to the theory, the theory must first be discussed. Consider the setup as shown in Fig. 1.4, in order to calculate the intensity at a point P, the contribution by an area element dS at the point a, to the optical disturbance at a point P is considered. Accounting for the unobstructed optical disturbance from S as well and using Eq. (1.4), yields:

$$U(P) = \frac{1}{i\lambda} \iint\limits_{\Sigma} \frac{Ae^{i(k\rho - \omega t)}}{\rho} \frac{e^{ikr}}{r} cos(\theta) \ dS \tag{1.7}$$

In the case where ρ_0 and r_0 are large compared to the size of the aperture, then $\cos{(\theta)} = 1$ and $\frac{1}{\rho r} = \frac{1}{\rho_0 r_0}$. The lengths of r_0 and ρ_0 are:

$$r = \sqrt{r_0^2 + y^2 + z^2} \tag{1.8}$$

$$\rho = \sqrt{\rho_0^2 + y^2 + z^2} \tag{1.9}$$

6

Using the binomial theorem to expand Eqs. (1.8) and (1.9) yields:

$$\rho + r \approx \rho_0 + r_0 + (y^2 + z^2)\frac{\rho_0 r_0}{2\rho_0 r_0} \tag{1.10}$$

Substituting Eq. (1.10) into Eq. (1.7) with $k = 2\pi/\lambda$

$$U(P) = \frac{Ae^{-i[k(\rho_0+r_0)\omega t]}}{i\lambda\rho_0 r_0} \iint_\Sigma e^{i2\pi y^2 \frac{(\rho_0+r_0)}{2\lambda\rho_0 r_0} + i2\pi z^2 e^{\frac{i\pi u^2}{2}} \frac{(\rho_0+r_0)}{2\lambda\rho_0 r_0}} \, dS \tag{1.11}$$

Introducing the dimensionless variables u and v

$$u = y\sqrt{\frac{2(\rho_0 + r_0)}{\lambda\rho_0 r_0}} \tag{1.12}$$

$$v = z\sqrt{\frac{2(\rho_0 + r_0)}{\lambda\rho_0 r_0}} \tag{1.13}$$

and substituting them into Eq. (1.11).

$$U(P) = \frac{\tilde{E}_u}{2} \int_{u_1}^{u_2} e^{\frac{i\pi u^2}{2}} \, du \int_{v_1}^{v_2} e^{\frac{i\pi v^2}{2}} \, dv \tag{1.14}$$

Equation (1.14) describes the optical disturbance at the point P, with $\tilde{E}_u$ the unobstructed disturbance at P. Equation (1.14) can be evaluated using the Fresnel integrals, $C(w)$ and $S(w)$:

$$\int_0^w e^{i\pi w'^2/2} dw' = C(w) + iS(w) \tag{1.15}$$

$$S(w) = \int_0^w sin\left(\frac{\pi w'^2}{2}\right) dw' \tag{1.16}$$

$$C(w) = \int_0^w cos\left(\frac{\pi w'^2}{2}\right) dw' \tag{1.17}$$

Using Eq. (1.15), where $C(w)$ and $S(w)$ are the Fresnel integrals as in Eqs. (1.16) and (1.17). Equation (1.14) can then be transformed into an intensity, by taking the absolute value and squaring, yielding Eq. (1.18):

$$I_p = \frac{I_u}{4}\{[C(u_2) - C(u1)]^2 + [S(u_2) - S(u_1)]^2\} \times \{[C(v_2) - C(v_1)]^2 + [S(v_2) - S(v_1)]^2\} \tag{1.18}$$

Equation (1.18) gives the intensity of the field at the point P on axis for a square aperture where I_u is the unobstructed intensity at the point P.

As the mathematics of calculating the optical disturbances at all points on a plane at point P is difficult, instead the aperture is moved by small displacements, with $\overrightarrow{SOP}$ fixed. This effectively achieves the translation of the origin, O, with respect to the fixed aperture. Thus, for each displacement new aperture coordinates y_1, y_2, z_1, and z_2 are generated and therefore new u_1, u_2, v_1, and v_2. Therefore the intensity at a point $P + \delta d$, where δd is the displacement,

can be calculated. This approximation holds for displacements that are small compared to the ρ_0 [20, 24, 25]. Using this method and Eq. (1.18) gives the theoretical curves in Fig. 1.5.

In φMC, the above experiment is simulated. A square slit is uniformly sampled in the x, and z direction in order to get the packets initial position. A random direction is then sampled, by uniformly picking a point on the detector screen. This ensures the algorithm does not waste time by calculating packets trajectories that are not registered by the detector. We assume a plane wave is incident on the aperture and each photon is given the same initial complex electric field.

The detector screen's distance from the aperture is then varied and the intensity on the screen is measured for $\sim 10^{10}$ photons released from the aperture as Huygens wavelets. For *Fresnel numbers* greater than 1.0, the number of bins is 300, covering a distance of 600 μm. For the case of Fraunhofer diffraction, the number of bins is 100 covering a distance of 6000 μm. The simulations take ~ 3 minutes for 10^{10} packets to be run on an Intel Xeon E3–1245 v5, 8 cores @ 3.5GHz machine. The number of bins, and photons packets simulated had to be increased for the cases where the Fresnel number was large (i.e the detector screen was near the aperture). This is due to the diffraction pattern becoming "noisy" and thus needs a higher resolution to accurately simulate. Fig. 1.5 shows the comparison between the theory and the φMC simulations.
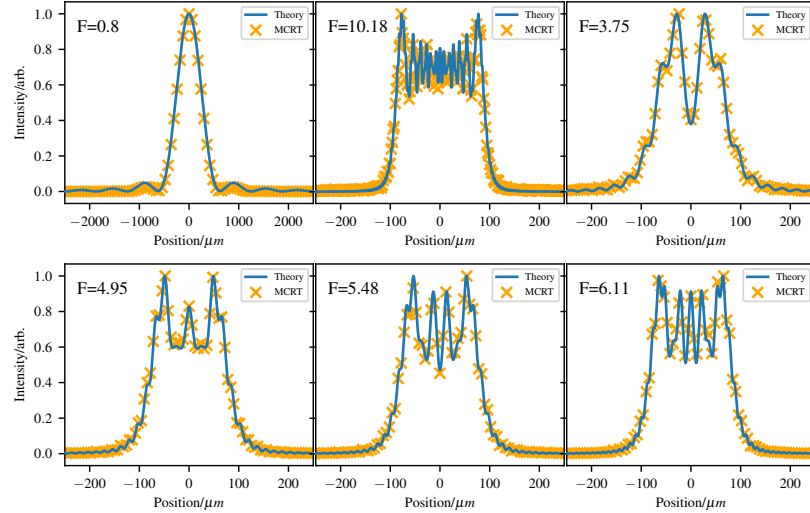
Figure 1.5: *Comparison of theory and simulation for diffraction through a square aperture in the Fresnel and Fraunhofer regimes.*

1.3   Gaussian Beams

Now that the method of tracking the complex phase of packets and using the Huygens-Fresnel principle has been verified against theoretical results, we can now turn our attention to modelling the propagation of beams that require the wave behaviour of light in order to either form or propagate. The first beam type we will examine is the Gaussian beam. Gaussian beams are important as most laser beams have the profile of the fundamental (TEM$_{00}$) Gaussian mode. This section will show that φMC can accurately model all the physical phenomena of Gaussian beams, within the MCRT regime.

Before discussing how φMC can model a Gaussian beam, the theory and various physical parameters of the beam must be described. The electric field of a Gaussian beam can be defined as in Eq. (1.19) [26]:

$$E(r, z) = E_0 \frac{w_0}{w(z)} e^{\frac{-r^2}{w(z)^2}} e^{-i(kz + k\frac{r^2}{2R(z)} - \varphi(z))} \qquad (1.19)$$

Where:

r is the radial distance from the optical axis $[m]$;

z is the axial distance from the beams waist $[m]$;

k is the wavenumber, $k = \frac{2\pi}{\lambda}$ $[m^{-1}]$;

E_0 is the electric field amplitude at the origin $[Vm^{-1}]$;

$w(z)$ is the radius of the beam at which the amplitude has fallen to $\frac{1}{e}$, at the distance z along the beam, Eq. (1.20) $[m]$;

w_0 is the waist radius $[m]$;

$R(z)$ is the radius of curvature of the beams wavefronts at z, Eq. (1.21) $[m]$;

and finally, $\varphi(z)$ is the Gouy phase at z, Eq. (1.22) [-].

Equations (1.20) to (1.24) give the definitions of key physical properties as outlined above or as shown in Fig. 1.6. z_r is the Rayleigh length, Eq. (1.23), and defines the point at which the beams waist grows to $\sqrt{2}$ times the size of the beam at its waist. The waist of the beam at the focal point is defined as Eq. (1.24), where f is the focal length and D is the $\frac{1}{e^2}$ diameter of the beam at the lens.

$$w(z) = w_0 \sqrt{1 + \left(\frac{z}{z_r}\right)^2} \qquad (1.20)$$

$$R(z) = z \left[1 + \left(\frac{z_r}{z}\right)^2\right] \qquad (1.21)$$

$$\varphi(z) = arctan\left(\frac{z}{z_r}\right) \qquad (1.22)$$

$$z_r = \frac{\pi w_0^2}{\lambda} \qquad (1.23)$$

$$w_0 = \frac{2\lambda f}{\pi D} \qquad (1.24)$$

$$(1.25)$$

With the physical properties of the Gaussian beam outlined, a Gaussian beam can now be modelled using our algorithm. To simulate a Gaussian beam, we set up the simulation as shown in Fig. 1.7. The simulated lens used is a convex-plano lens, with radius of curvature, 4.6 mm, thickness, L_t, of 2.2 mm, and working distance, W_d, 8.5 mm. A Gaussian beam wavelength 488 nm and $\frac{1}{e^2}$ waist diameter 0.5 mm, is incident on the lens. Using Eq. (1.24) yields the size of the focal spot as $3.11\mu m$.

To model the lens in φMC the photons initial z position is set just in front of the lens. The x and y are randomly sampled from a Gaussian distribution with a waist of $\sqrt{2}w_0$. The factor of $\sqrt{2}$ accounts for the conversion from intensity to electric field beam waist. This is because the electric field is $\propto \exp\left(\frac{-r^2}{4\sigma'^2}\right)$, and the intensity is $\propto e^{\frac{-r^2}{2\sigma^2}}$. Thus for the input electric field waist to be equal to the intensity waist, i.e $\sigma' = \sigma$, $\sigma' = \sqrt{2}\sigma$. The packet is given an electric field of the form Eq. (1.1), with $P = 1$ mW, and $A = \frac{1}{2}\pi w_0^2$.

9
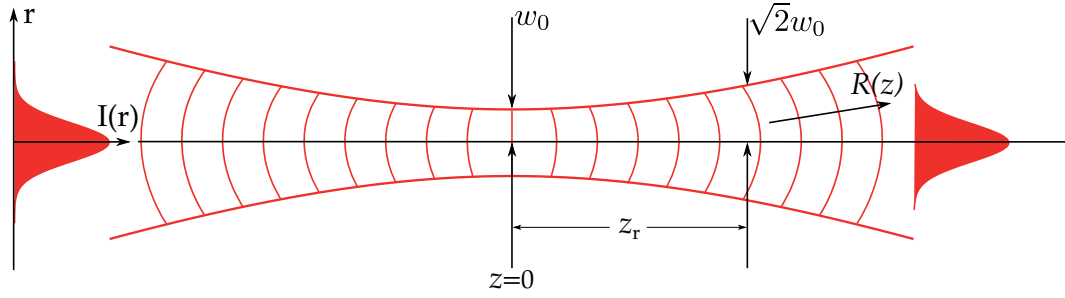
Figure 1.6: *Illustration of a Gaussian beam focusing to its waist then diverging away. Image shows the various defined properties of a Gaussian beam along side the radius of curvature changing direction at the waist.*
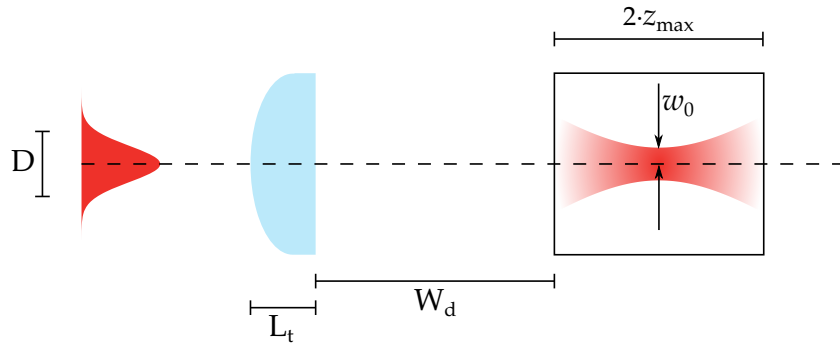
Figure 1.7: *Simulation setup of focusing a Gaussian beam through a lens. Lens is convex-plano and is modelled on ThorLabs LA4249 UV fused silica lens [27]. L_t is the lens thickness, D is the $\frac{1}{e^2}$ input beam diameter, W_d is the working distance or back focal length, $2 \cdot z_{max}$ is the depth of the medium, and w_0 is the beam waist.*

The photon is then propagated to the surface of the convex side of the lens. This is achieved by finding the intersection of a sphere, which represents the convex side of the lens, and the packets path. With the packet on the surface of the lens, Fresnel coefficients are calculated to determine if the packet is reflected or refracted. If the packet is reflected the packet is killed and the process starts again. If the packet is refracted, and moved in the new direction to the planar surface of the lens. The new direction vector is calculated using a vector version of Snell's law, as shown in **??**. The packets are then uniformly sampled onto the surface of the voxel medium and the usual MCRT method is used to propagate the packet whilst tracking the phase.

Figure 1.8 shows the comparison of theory and *in-silico* experiment, with excellent agreement between the two.

φMC also correctly models the change of direction of the radius of curvature, $R(z)$, as is predicted by theory. This can be seen in Fig. 1.9

φMC can also model spherical aberrations caused by lenses. Figure 1.10 shows aberrations caused by a plano-convex lens.

This section has shown that Gaussian beams, and their physical phenomena can be accurately modelled using φMC. A convex-plano lens was used to focus a Gaussian beam, but it is simple to implement other lenses given a triangulated mesh of the lens or an equation that describes the shape of the lens, e.g an aspheric lens.
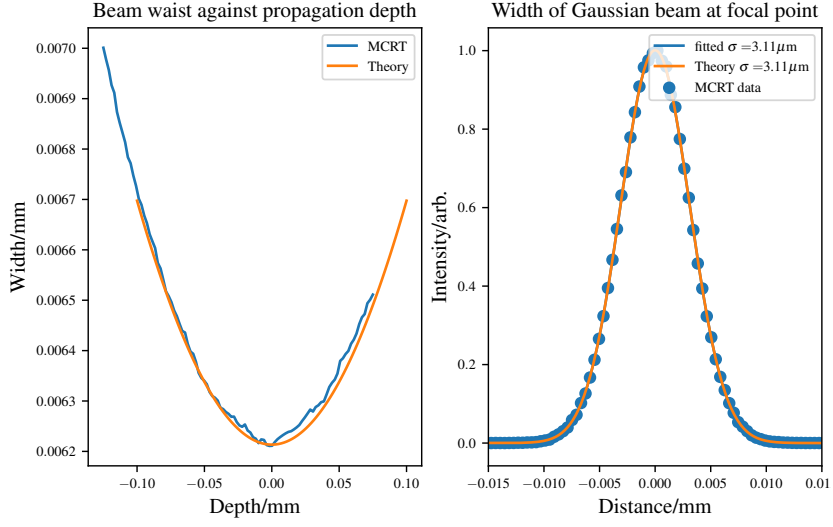
Figure 1.8: *Results of in-silico experiment of focusing a Gaussian beam though a convex-plano lens.*
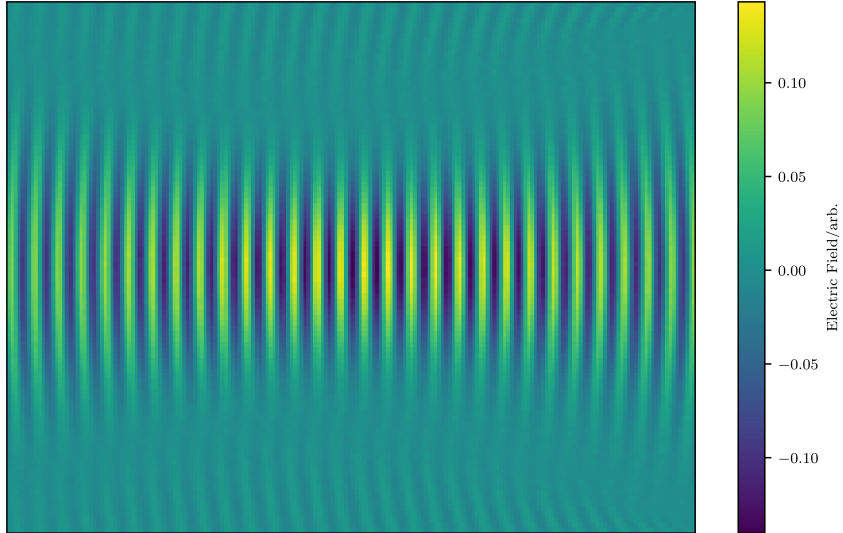
Figure 1.9: *Slice through the real part of the complex electric field of the in-silico experiment as in Fig. 1.7. Figure shows the radius of curvature changing direction at the waist as predicted by theory.*
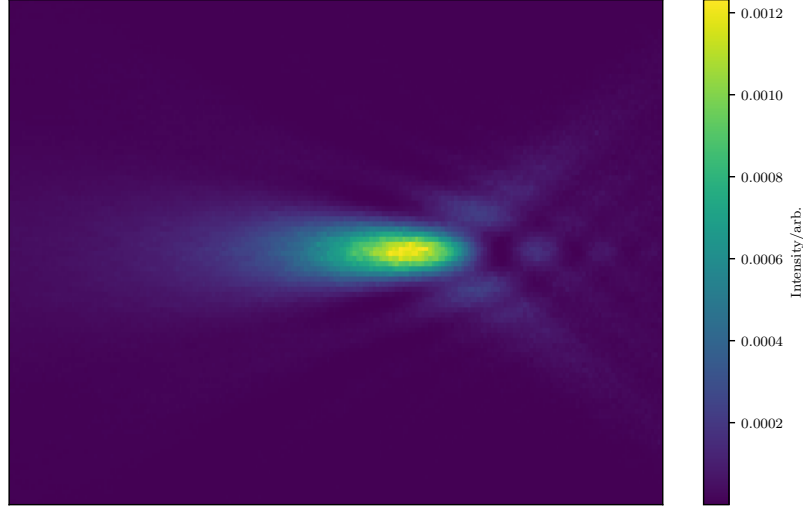
Figure 1.10: *Illustration of φMC's ability to model spherical aberrations. Image generated using same setup as in Fig. 1.7, but with $D = 1.5$ mm.*

1.4 Bessel Beams

Bessel beams have been the subject of intense research since their discovery in 1987 [28, 29]. Durnin noticed that the solution to the Helmholtz equation of the Bessel type were independent of the direction of propagation. This means is that the central core of the beam is generally more diffraction resistant when compared to a Gaussian beam with a similar spot size. Bessel beams also have a property of "self-healing", this means if an obstruction is placed in the path of the central lobe of the Bessel beam, the Bessel beam can then "heal" and reform past the obstruction [30]. However it is physically impossible to create a "real" Bessel beam, as the Bessel beam can have infinite rings, which each carry the same amount of power, thus would require infinite amount of power [28]. Therefore all Bessel beams that are created experimentally are quasi-Bessel beams which are similar to their theoretical counterpart over a finite distance [28].

These two properties make Bessel beams an attractive avenue of research, as novel solutions to imaging problems. There is also some debate among physicists as to whether these phenomena are justly labelled, or if they glib terms used to make Bessel beams seem better than they are [31–35].

1.4.1 Theory

As before with the Gaussian beam, the theory behind the Bessel beam must be discussed before we can model the beam in φMC. The electric field can be described using Eq. (1.26) [36]:

$$E(r,z) = E_0 \sqrt{\frac{2\pi k z w_0 \sin(\beta)}{z_{max}}} \, \exp^{\left(-\frac{z^2}{z_{max}^2} - \frac{i\pi}{4}\right)} \, J_0\left(kr\sin(\beta)\right) \, \exp^{(ikz\cos(\beta))} \tag{1.26}$$

Where:

k is the wavevector, $k = \frac{2\pi}{\lambda}$ [m];

z is the propagated distance [m];

12

β is the angle the wavefront propagates at (see Fig. 1.11) $[rad]$;

w_0 is the $\frac{1}{e^2}$ width of the input Gaussian beam $[m]$;

J_0 is the Bessel function of the first kind, zeroth order;

r is radial distance from the optical axis $[m]$.

Equation (1.26) gives the electric field for a Bessel beam. The intensity can be calculated using:

$$I(r, z) = \frac{c\epsilon_0 |E|^2}{2} \tag{1.27}$$

Using the definition total power transmitted by a beam as:

$$P = \frac{\pi I_0 w_0^2}{2} \tag{1.28}$$

Where I_0 is defined as on axis intensity of the incident Gaussian beam.

$$I_0 = \frac{c\epsilon_0 E_0^2}{2} \tag{1.29}$$

Substituting Eqs. (1.26), (1.28) and (1.29) into Eq. (1.27) yields:

$$I(r, z) = \frac{4k_r P}{w_0} \frac{z}{z_{max}} J_0^2 (k_r \ r) \exp^{\left(-\frac{2z^2}{z_{max}^2}\right)} \tag{1.30}$$

Where:

k_r is the radial wavevector, $k_r = k \ sin(\beta)$;

P is the power of the incident Gaussian beam.

A Bessel beam can be formed by an axicon lens or by diffraction through a ring. All the simulations of Bessel beams in this thesis use the axicon method of generating a Bessel beam, thus only axicons will be discussed. Figure 1.11 shows the geometry of a Bessel beam formed by an axicon. Using simple geometry and Snell's law the following equations can be derived to describe various properties of a Bessel beam formed by an axicon [37].

The propagation depth of a Bessel beam is defined as the distance from the tip of the axicon to the end of the "Bessel region". However in reality the Bessel beam will continue to propagate slightly passed this depth. Equation (1.31) shows the propagation depth of a Bessel beam where cot is the cotangent function ($cotx = \frac{1}{\tan x}$).

$$z_{max} = R \left(cot \left(\beta \right) - tan \left(\alpha \right) \right) \tag{1.31}$$

The propagation angle of the conical waves, β can be calculated using Snell's law and α the angle of the axicon:

$$\beta = arcsin \left(n \ sin \left(\alpha \right) \right) - \alpha \tag{1.32}$$

The central core of a Bessel beam is defined as the distance to the first zero of the Bessel beam. Equation (1.33) shows the radius of the core, where 2.405 is derived from position of the first zero of the Bessel function.

$$r_o = \frac{2.405}{k \ sin \left(\beta \right)} \tag{1.33}$$

Finally, the spacing between Bessel beam rings is:

$$\Delta \rho = \frac{\lambda}{2 \ sin \left(\beta \right)} \tag{1.34}$$

1.4.2 Validation

To ensure that the method described in Section 1.2 works as intended for Bessel beams several tests are run against theoretical expressions and experimental data.
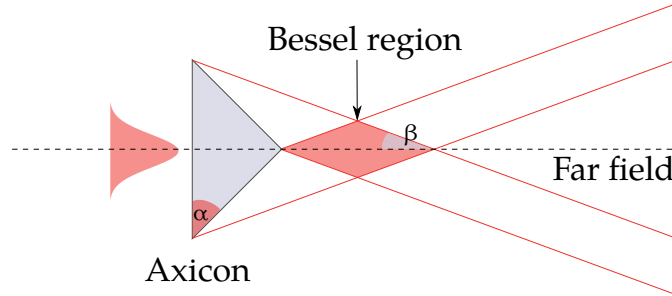
Comparison to theoretical Bessel beam

To compare against a theoretical Bessel beam, a Bessel beam is modelled in φMC, and propagated through air into the "Bessel region" and then propagated into the far field to ensure the beam follows the theory in both these regions.

Figure 1.11 shows the set-up for the *in-silico* experiments. The Bessel beam is created with an axicon (conical) lens with an opening angle (α) of 5°, and a radius of 12.7 mm. The input beam is Gaussian in profile with a $\frac{1}{e^2}$ diameter of 1 mm, and a wavelength of 488 nm. The Bessel beam is then propagated to a detector screen 10 mm away from the tip of the axicon, which is in the middle of the "Bessel region" for the first test. For the second test the Bessel beam is propagated past the "Bessel region" into the far field. The detector screen has a size of 40 μm × 40 μm with a bin resolution of 1 μm. 8^{10} photon packets were simulated taking ~ 1 hour on an 8 core Intel Xeon 3.5Ghz machine.

Equation (1.30) gives the profile of a theoretical Bessel beam at a depth z_{max}, this is plotted against the simulation when $\frac{4k_r Pz}{w_0 z_{max}} e^{-2\left(\frac{z}{z_{max}}\right)^2} = 1$, with the simulation similarly normalised to the maximum intensity of the image generated. Figure 1.12 shows this comparison.

Figure 1.13 shows the profile of the Bessel beam in the far field, where the theory predicts it becomes a circular beam. φMC can also model the self-healing property of Bessel beams, this is shown in Fig. 1.14.

Figure 1.11: *Geometry of a Bessel beam, generated by an axicon lens. β is the angle with the optical axis, and the angle of the conical waves. α is the axicon angle.*
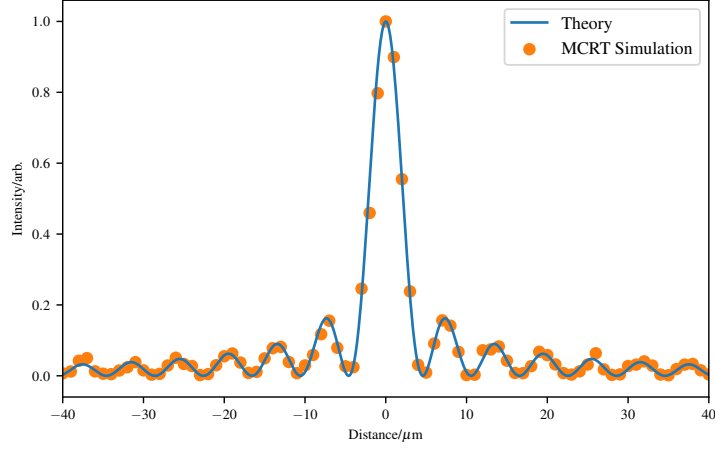
Figure 1.12: *Comparison of theoretical and MCRT simulation of a Bessel beams, with intensity normalised. The results from φMC show good agreement with the theory.*
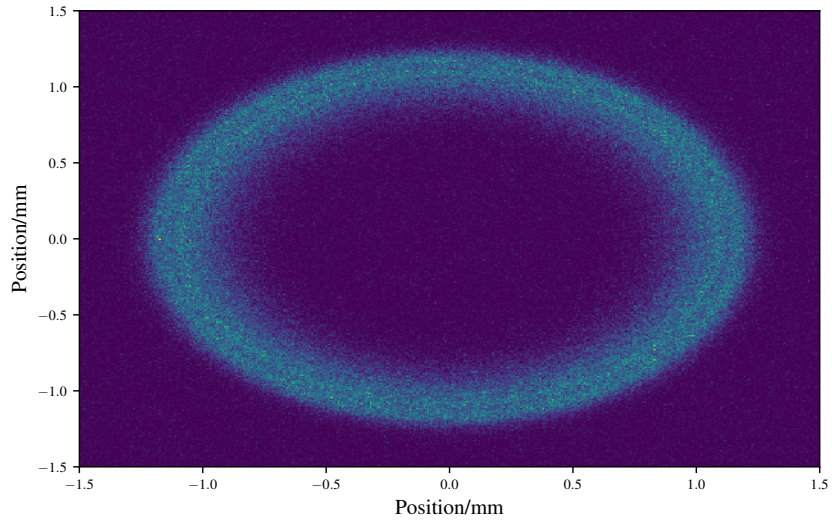
Figure 1.13: *Bessel beam in the far field.*

15
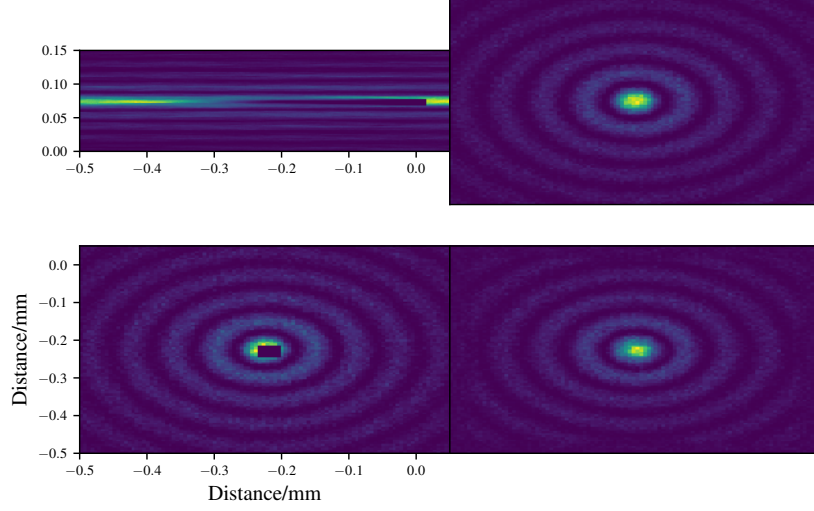
Figure 1.14: *Illustration of the Bessel beams self-healing property. Highly absorbing cube placed near the top of the medium. Figure shows that the Bessel beam forms further down the optical axis.*

Comparison to experimental data

To ensure our algorithm works in turbid media, we carried out an experiment where a Bessel beam was propagated through a medium of varying turbidity. A laser, wavelength 488 nm, with a Gaussian profile is shone on an axicon lens, with angle 5°. The laser beam had a $\frac{1}{e^2}$ diameter of 2 mm. The Bessel beam was allowed to propagate through the air for 10 cm before entering a cuvette of side 2 mm. The cuvette was filled with 500 μL of water, and various volumes of a scattering agent added. The scattering agent used is intralipid 20 % (Sigma-Aldrich), which is diluted as shown in Table 1.1. Figure 1.16 shows the optical properties of Intralipid 20 %. Dilutions of Intralipid are kept below 2% scattering particle concentration, so that the scattering exhibited by the intralipid is in the independent scattering regime. This allows the linear scaling of the optical properties by concentrations [38–40]. Images of the Bessel beam as it emerges from the cuvette are taken for comparison with our algorithm. Figure 1.15 shows the experimental set-up.
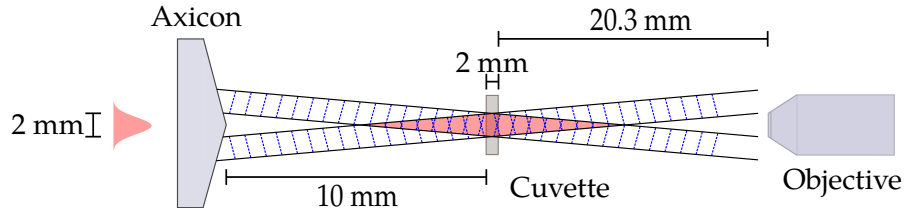


Figure 1.15: *Experimental set-up for propagating a Bessel beam through a cuvette filled with varying concentrations of Intralipid 20%. Bessel beam is imaged by an 20× objective lens and a Grasshopper 3 camera.*

To model within φMC, we simplify the experimental setup considerably. The simulation models the propagation of a photon packet through the axicon to its conical surface. On the

| Volume/μL | | Intralipid concentration | | Optical properties |
Intralipid	H_2O	Volume/%	Scattering particle/%	Scattering coefficient/m^{-1}
0	500	0.00	0.00	0.00
2	500	0.39841	0.0908	557.14
4	500	0.79365	0.1816	1114.28
6	500	1.18577	0.2724	1671.42
8	500	1.57480	0.3632	2228.56
10	500	1.96078	0.4534	2785.71
12	500	2.34375	0.5448	3342.84

Table 1.1: *Intralipid solutions used for experiment, see also Fig. 1.16.*
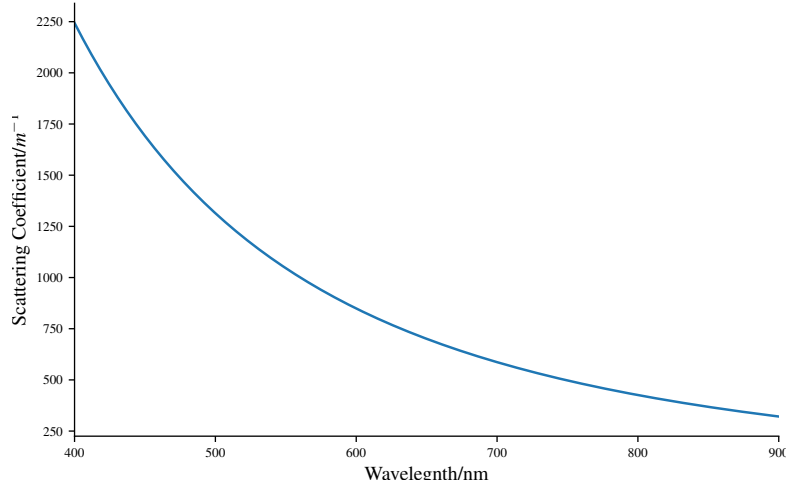
Figure 1.16: *Scattering properties of 20% Intralipid [41].*

conical surface the Huygens-Fresnel principle is invoked, and the packet is sampled onto the surface of the medium (cuvette). The sampling of the photon onto the surface of the medium, speeds the algorithm up, as it does not need to simulate the photons that would "miss" the medium. From there the usual MCRT method propagates the packet through the medium while tracking its phase, and scattering the packet until it leaves the medium. If the packet leaves the medium to any side other than the far side of the cuvette (e.g any side of the cuvette not facing the objective lens), then it is discarded. If the packet leaves the medium on the objective lens facing side, then the packet is recorded by its phase onto an area element. For each intralipid concentration 6.4×10^{10} photons are run over 64 cores, taking ~ 3 hours for the $12\mu L$ intralipid volume. Once all the packets have been run, the phase is converted into intensity, as in Eq. (1.3), but in 2D.

Figure 1.17 shows the results from the experiment and simulation. The simulation shows good agreement with experimental data within experimental and simulation uncertainty.

Discussion

Originally the medium was modelled as in the experiment, a 2 mm^3 volume. The image created was thus a 2001×2001 with a resolution of 1 μm. To achieve a good signal to noise ratio for this setup 6.4×10^{12} packets needed to be run, taking ~ 70 hours on a computer cluster using 64 cores. This was sufficient to get a good signal to noise ration on all the simulations up to
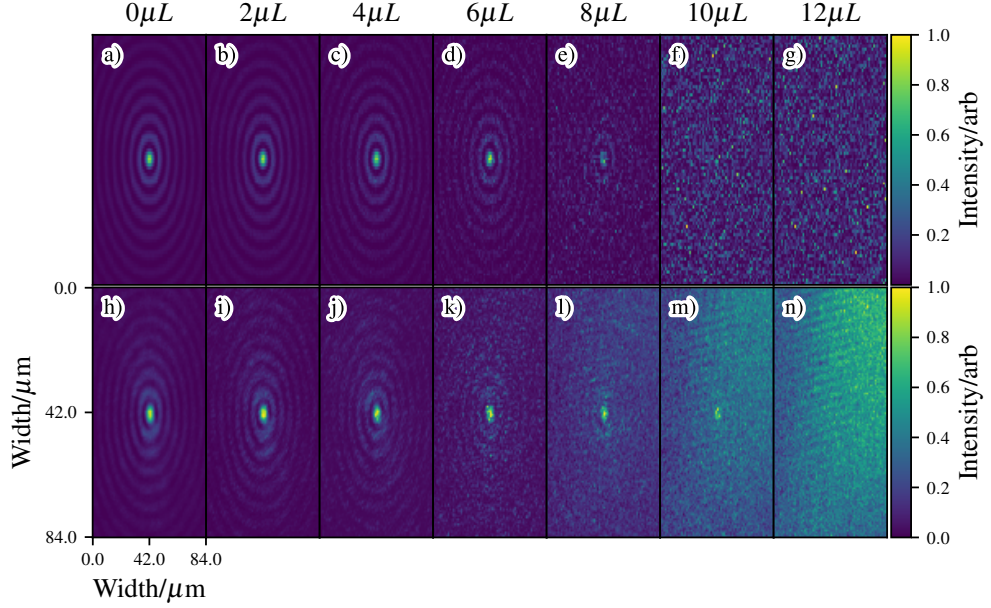
Figure 1.17: *Comparison of experimental and simulation data for propagation of a Bessel beam produced by an axicon, through mediums of various turbidity. Images a) to g) is the data from φMC, and h) to n) are the experimental data. Volumes along the top is the volume of Intralipid in each solution as in Table 1.1. All images cropped so they are the same size and normalised to the maximum value in each image.*

6 μL. However the amount of packets needed to get a good signal to noise ratio for 8 μL and above was prohibitively computationally costly. Therefore the modelled medium was shrunk in the x and y directions giving: $0.5\ mm \times 0.5\ mm \times 2.0\ mm$. This allowed a smaller image (501 $\times$ 501), whilst keeping the same resolution. Shrinking the medium also has the benefit that the photons are confined closer to the image plane, thus ensuring more photons are hit the plane in comparison to the larger medium.

Shrinking the mediums size does have some draw backs. First the Bessel beams propagation depth rely on the input beams width see Eq. (1.31). The input beams width was kept constant between the shrinking of the volumes size. However shrinking the mediums size in the x and y directions gives the same effect as using a smaller input beam. Therefore the x and y dimension were carefully chosen such that the Bessel beam would still form a Bessel beam at the image plane. The second issue with shrinking the medium is that some packets may be lost. This means that in the larger medium a packet may scatter towards an x or y medium wall and then scatter back into the centre of the medium and then is recorded. However this same packet in the smaller medium would be lost as the packet would exit the medium and ceased to be tracked. It is not expected that this will cause much of an issue as any scattering event already degraded the quality of the beam, as that packet is no longer coherent with the rest of the packets, thus it will not contribute positively to the Bessel beam. To ensure this is not an issue, results from a larger medium are compared to that of the smaller medium in Fig. 1.18. The larger and smaller medium yield the same results (within Monte Carlo noise) for Intralipid volumes less than 8 μL. At 8 μL the smaller medium has a Bessel beams central core, whilst the larger

medium is noisy, and forms no Bessel beam. This test has shown that shrinking the medium allows accurate modelling of the propagation of a Bessel beam through a turbid medium while using less computational resources.
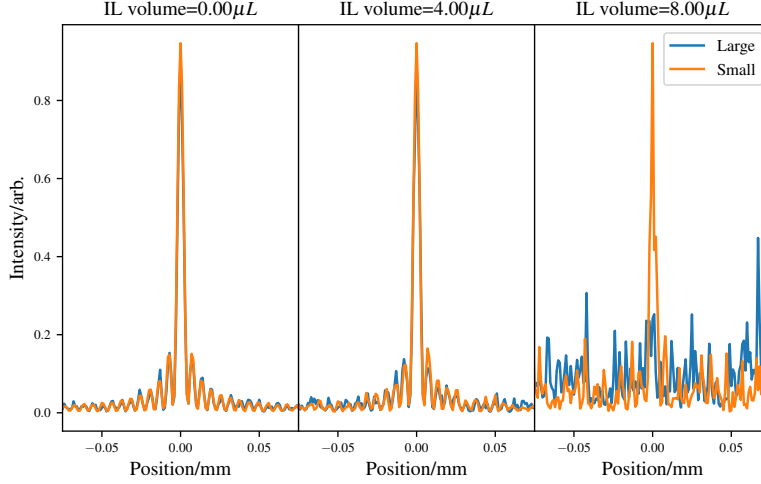
Figure 1.18: *Comparison of a larger medium, $2 \ mm^3$ versus that of a smaller medium, $0.5 \ mm \times 0.5 \ mm \times 2.00 \ mm$.*

1.5 Higher Order Bessel Beams

Higher order Bessel beams (HOBBs), are Bessel beams where the electric field has an extra term of $e^{-il\varphi}$, as shown in Eq. (1.35), and $l \neq 0$. HOBBs have found use for optical trapping targets that are reflective/low refractive index, and optical manipulation [42,43]. Our technique outlined in the preceding sections, can also be applied to arbitrary higher order Bessel beams.

As before, the electric field of a lth order Bessel beam is:

$$E(r, \varphi, z) = E_0 J_l(k_r r)e^{-ik_z z}e^{-il\varphi} \tag{1.35}$$

Where:

l is the order of the beam [-];

$k_z^2 + k_r^2 = k^2$, where k^2 is the wavevector $[m^{-1}]$;

r, φ, and z are the cylindrical coordinates $[m, rad, m]$;

and J_l is the l-order Bessel function of the first kind [-].

To generate higher order Bessel beam, a helicon is used. A helicon (shown in Fig. 1.19) is an axicon attached to a helix phase delay element. The helical element imparts a helical phase delay to photon packets as they pass through the element.

The distance travelled though the helicon is shown in Eqs. (1.36), (1.37) and (1.39) [44]. h_1 is the path length travelled by a photon through the helical element. h_2 is the path through an axicon, and Δh is the height of the helical discontinuity.

19

$$h_1 = \frac{l\phi\lambda}{(n-1)2\pi} \tag{1.36}$$

$$h_2 = r\,tan(\alpha) \tag{1.37}$$

$$h_3 = h_1 + h_2 \tag{1.38}$$

$$\Delta h = \frac{l\lambda}{n-1} \tag{1.39}$$

Where ϕ is the azimuthal angle, r is the radial position, l is an integer that describes the order of the Bessel beam, and α is the axicon angle.

The path length in the above equations can be converted into a phase delay by considering the transmission functions of the individual elements [45–48]:

$$T_1(\varphi) = e^{-ik(n-1)h_1} = e^{-il\phi} \tag{1.40}$$

$$T_2(r) = e^{-ik(n-1)h_2} = e^{-ik_r r} \tag{1.41}$$

$$T_3(r,\varphi) = T_1 * T_2 = e^{-ik_r r - il\phi} \tag{1.42}$$

$$\tag{1.43}$$

Where T_1 is the transmission function for the helical element, T_2 is the transmission function for the axicon, and T_3 is the total transmission function. Using the small angle approximation for β and Eq. (1.32), and knowing $k_r = sin(\beta)$ yields the phase delay as a function of angle and radial position:

$$\varphi(\phi, r) = k(n-1)r\alpha + l\phi \tag{1.44}$$

To implement a helicon in the φMC algorithm, an additional helical phase delay is added. The additional delay is implemented by adding $l\phi$ where $0 < \phi < \frac{2\pi}{l}$. An actual helix element is not modelled explicitly in the code, but rather just the phase delay. This method is similar to using a spatial light modulator in an experiment to impart a phase delay on a beam.

Figure 1.20 shows the comparison between theoretical higher order Bessel beam and the higher order beam simulated by φMC.
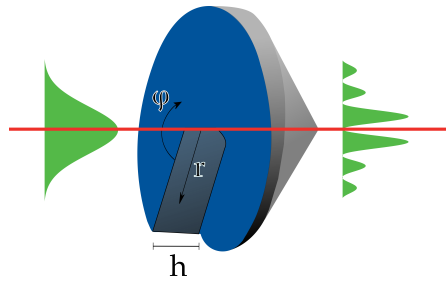
Figure 1.19: *Helical delay element attached to an axicon. The Axicon introduces a radial delay in addition to that of the helical element. If the input beam is a Gaussian, the output beam is a higher order Bessel beam, $l > 0$.*
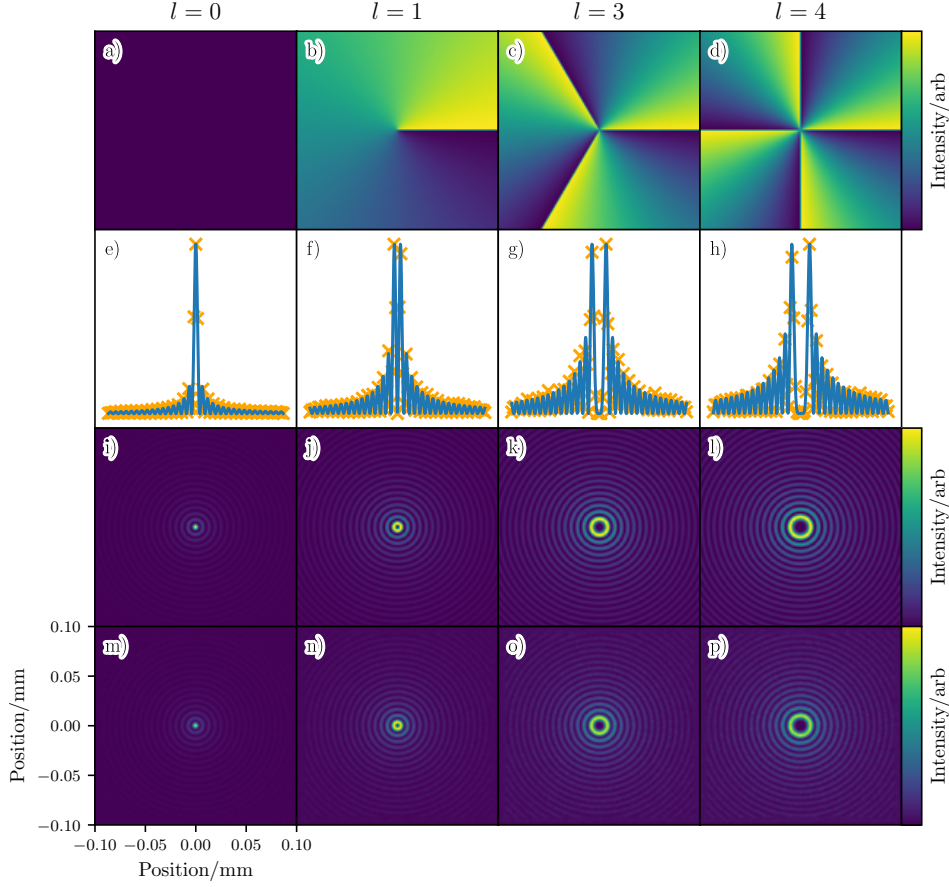
Figure 1.20: *HOBBs. a) to d) show the phase shift due to the helical element. e) to h) show line plots of the simulation data compared to the theory. i) to l) and m) to p) show the higher order Bessel beam images for theory and simulation data respectively.*

1.6 Comparison

As Bessel and Gaussian beams are radically different from one another it is hard to directly compare the two beams. Gaussian beams carry all their power in the "central core" of the beam, whereas in a Bessel beam, it carries the same amount of power in each ring. Bessel beams also have a much larger depth of focus than Gaussian beams. This section attempts to compare the two beams, to predict which beam preform better in a heavily scattering medium using φMC. Bessel beams are expected to preform better than Gaussian beams, due to their self-healing properties and non-diffractive core, this section aims to quantify how this property may or may not help penetration though highly scattering medium.

As mentioned, Bessel beams and Gaussian beams are not alike, so to ensure a fairer comparison the Bessel beams central core width is set to that of the Gaussian beam's waist.

$$r_0 = \frac{\kappa}{k \, sin\beta} \tag{1.45}$$

Where κ is a constant that determines the metric used to measure the Bessel beam's core, and the other symbols have the same meanings as before. For $\kappa = 2.408$ the radius is measured from the maximum of the core to the first zero of the Bessel beam. $\kappa = 1.75$ measures the Bessel beam's core from the maximum to $\frac{1}{e^2}$ of the maximum. For both beams central cores to be equal, the axicon used to generate the Bessel beam is adjusted. This is achieved by calculating the "correct" α based upon the optical setup used to focus the Gaussian beam. Using the small angle approximation[†] and $\kappa = 1.75$ we can compare the Bessel beam's core radius to a Gaussian beam's waist:

$$\frac{1.75\lambda}{2\pi sin\beta} = \frac{2\lambda f}{\pi D} \tag{1.46}$$

$$\alpha = \frac{1}{n-1} asin\left(\frac{1.75D}{4f}\right) \tag{1.47}$$

Where α axicon angle as before, n is the refractive index of the axicon, D is the $\frac{1}{e^2}$ diameter of the incident Gaussian beam on the lens, and f is the focal length of the lens used to focus the Gaussian beam. Both D and f are properties of the optical system used to focus the Gaussian beam. The lens used to focus the Gaussian beam is the same as used in the previous section to validate that φMC can model a Gaussian beam, a convex-plano lens, with radius of curvature 4.6 mm, a working distance of 8.5 mm and thickness of 2.2 mm.

The first comparison carried out between the Bessel and Gaussian beams is to use the same power to generate both beams. The beams are the propagated through mediums of varying degrees of Intralipid solution. Volumes of 0.0, 26, 52, 78, and 104 μL are used of Intralipid in 500 μL of water. The medium has a volume of 0.1 $mm \times 0.1$ $mm \times 0.2$ mm, and voxel resolution of 1 μm. For both beams a wavelength of 488 nm and a power of 1 mW is used. One hundred million packets are simulated for each simulation. The results of this are shown in Figs. 1.21 and 1.22

The results show that for the same power, Gaussian beams propagate deeper into the medium compared to Bessel beams. This is to be expected as in a Gaussian beam all the power is in its "central core", whilst the power is evenly distributed between all the Bessel beam's rings. Therefore, for a second comparison the power given to the Bessel beam is such that the central core maximum matches that of the Gaussian beam's at its focus for the case where there is no scattering. To achieve this the Bessel beam was given $\sim 15\times$ the power given to the Gaussian beam. The results of this comparison are illustrated in Fig. 1.23.

These results show as expected that the Bessel beam now preforms comparably with the Gaussian beam in lower scattering media, with a drop off in performance in the higher scattering media.

[†]for small α and β: $\beta = (n-1)\alpha$.
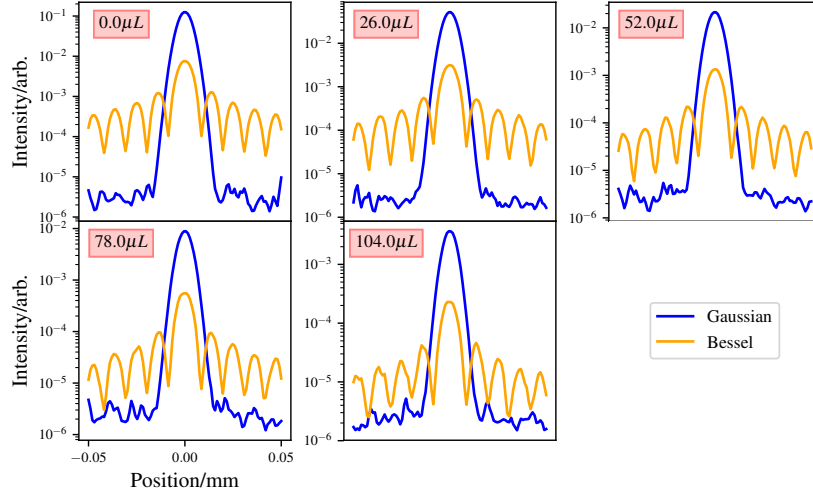
Figure 1.21: *First comparison of Bessel and Gaussian beams, with equal power used to generate both beams. Plots taken at the Gaussian beams focus. The maxima at the sides of the Gaussian beam in the $0.0\mu L$ plot are due to simulation effects, mainly the small size of the medium not allowing photons from further off the optical axis to interfere destructively.*
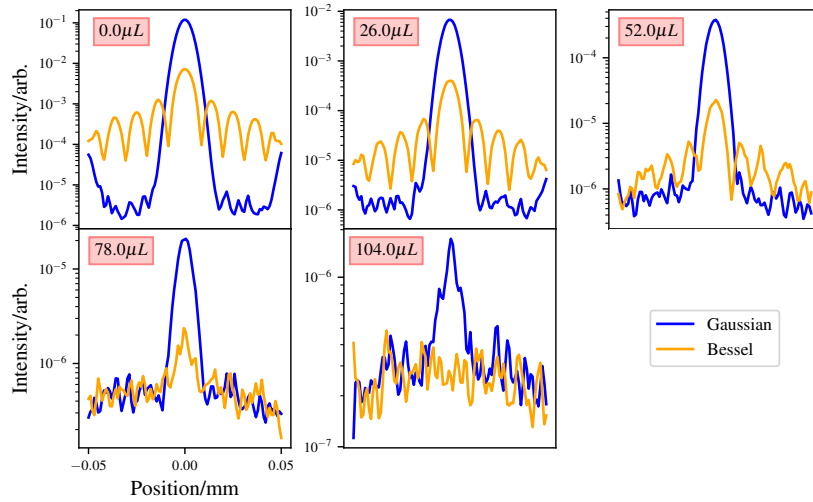
Figure 1.22: *First comparison of Bessel and Gaussian beams, with equal power used to generate both beams. Plots taken at the bottom of the simulated medium.*
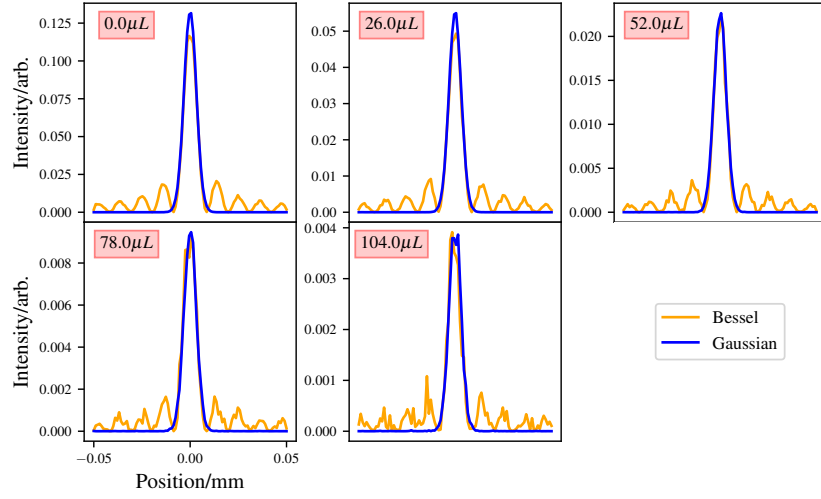
Figure 1.23: *Second comparison of Bessel and Gaussian beams for the case where the power given to each beam, yields the same maximum at the Gaussian beams focus. These plots are taken from the Gaussian beams focus*
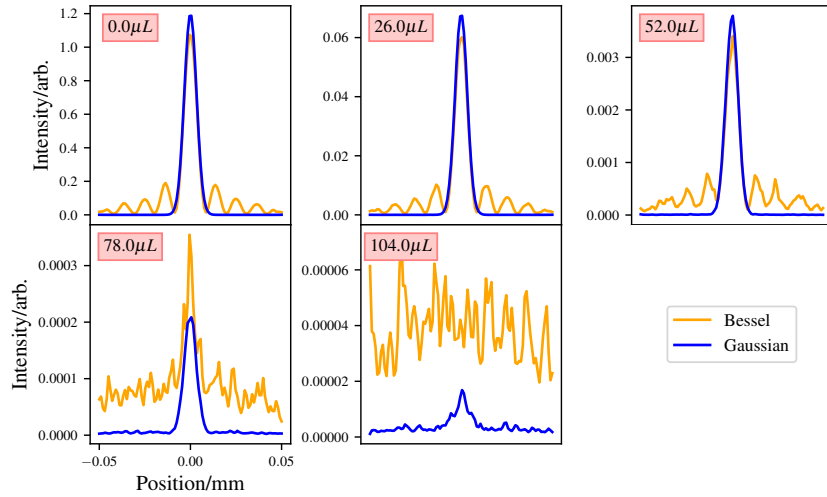
Figure 1.24: *Comparisons of unequal powered beams at the bottom of scattering medium.*

1.6.1 Discussion

For equal power beams in the previous section, Gaussian beams preform, "better" in the highly scattering mediums. Though this is expected due to the Bessel beams property that the power in the beam is spread evenly over its rings. Thus the power in the central lobe is much less than that of the Gaussian beam.

To give a slightly more fair comparison, the Bessel beam was given $15\times$ more power than the Gaussian beam. This gave a comparable intensity between the beams at the location of the Gaussian beams focus. In this case, the Bessel beam appears to preform better in a highly scattering medium, as shown in Fig. 1.24. The Bessel beam shows comparable intensity with the Gaussian beam in the first three mediums, though the Gaussian beam out preforms the Bessel beam in the higher scattering media. It would appear that the Bessel beams self-healing property does not help a Bessel beam propagate through a highly scattering medium. Figure 1.25 shows how the Bessel beam may become degraded due to scattering. As photons propagate though the medium they interfere with one another constructively and destructively to form a Bessel beam. However if enough photons are scattered, then the Bessel beam becomes degraded and thus no longer is a Bessel beam, as these photons are no longer coherent with the rest of the beam, so they act as a negative factor in the beams formation. Another reason that the "self-healing" property of the Bessel beam does not "save" the beam from scattering is that the "self-healing" is not self-healing. The self-healing in reality is just photons from further off the optical axis forming the Bessel beam further down the optical axis, e.g the photons that are impeded by the blockage are stopped, but the photons that are not impeded form a Bessel beam as expected. If you placed a blockage in front of the Bessel beam larger than the width of the input beam, then the Bessel beam would not form at all.

Bessel beams do have their positives, their self-healing property does help "reform" the beam past small blockages, and their depth of field is superior to an equivalent Gaussian beam, as their central cores is "non-diffractive".
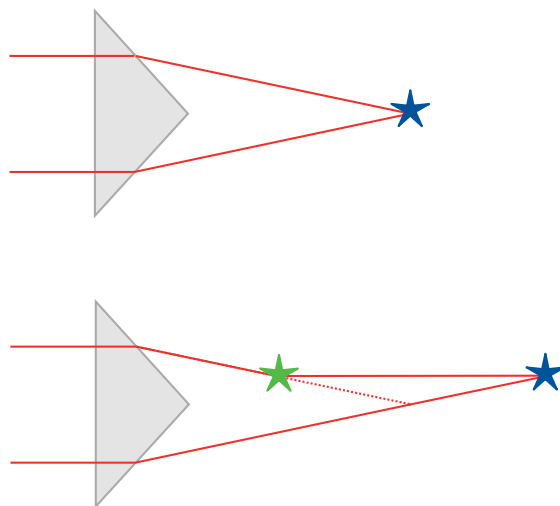
Figure 1.25: *Illustration of how a Bessel beam becomes degraded due to scattering. Top image shows how two photons propagate through the axicon and constructively interfere to produce a Bessel beams. Bottom imgae shows how scattering can affect this process.*

1.7 Conclusion

This chapter has shown that it is possible to transform a traditional particle behaviour MCRT method into a method that allows the simulation of quasi-wave/particle behaviour of photons. This is achieved by introducing two principles to the algorithm: the tracking of complex phase of each packets and the Huygens-Fresnel principle. The tracking of the complex phase of each packets allows interference of the quasi-wave/particles to be simulated. The Huygens-Fresnel principle allows diffraction to be accurately modelled. φMC has be thoroughly validated against several experiments where modelling the wave behaviour of light is vital to the experiment. Alongside the above, presented in this chapter is the modelling of complex beam types: Gaussian and Bessel beams. Both beams types have been validated against either both theoretical and experimental results. Finally Gaussian beams and Bessel beams were compared against one another in a highly scattering medium, where Bessel beams appear to give better performance. However, φMC is not a silver bullet for modelling these complex beams in a scattering medium. Depending on the problem at hand, the computational load can be excessive. For example, if you want to know the intensity of the beam at all locations though a large ($> 1mm^3$) scattering medium with a complex 3D structure, then the time taken to get a good signal to noise ration may be computationally prohibitive. Though it is expected that in most cases the intensity is not needed at all locations in a medium, and an image is all that is need to be calculated, then even in a complex 3D structure φMC should preform better than the methods listed at the start of this chapter[‡]. Were φ excels is that it can accurately model scattering effects on the propagation of complex beams through scattering media, if that media is simple in terms of structure.

[‡]Though to achieve better performance with the current code, adaptive mesh grids would have to be implemented.

Appendices

Appendix A

Detected Light Fluence Tracking Method

Most the fluence graphs presented in this thesis shows the fluence of the incident light throughout the simulated medium. However, there are problems where tracking the fluence of the detected light maybe useful, though this quantity is not straight forward to track. The current method of tracking fluence, is to add pathlengths, calculated as the packet moves from voxel to voxel to a 3D array. This method obviously cannot determine which packet will be detected before the packet is detected, therefore a new method must be devised. This new method tracks the coordinates, direction vectors, random optical distance and fluorescent source of the packet using a stack. A stack is a commonly used abstract data structure, and is a collection of elements. In this case the elements are the coordinates, direction vectors, optical distance and fluorescent source. A stack has two main operations, pop and push. The push operation adds a new element to the collection, and the pop operation removes the most recently added element from the collection. This is known as last in first out (LIFO). Figure A.1 shows these two operations in action.
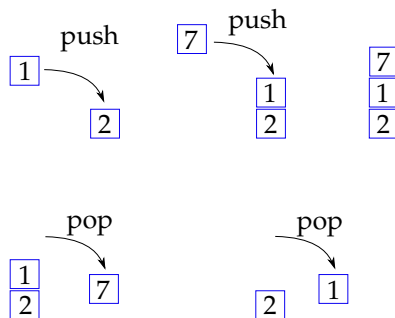
Figure A.1: *Example of the push and pop operation on a stack. The first operation add the integer 2 to the stack. The second operation push 7 to the stack. The last operation pops the 7 from the stack.*

The progress of each packets is pushed onto the stack, as it is propagated through the simulated medium. As mentioned above the packets coordinates, direction vectors, optical depth, and fluorescent source are the quantities pushed to the stack. These quantities are pushed to stack every time an interaction event occurs. When a packet is terminated, either via absorption

or it leaving the medium, the packets details are removed from the stack. This occurs unless the packet is detected. If the packet is detected then the information remains on the stack. This whole process repeats until all the packets have been run. Once all the packets have been run, the packets are "replayed". This is achieved by popping the information off the stack and passed to the inttau2 routine. The packet is the propagated again, this time recording the fluence as done in most of the chapters in this thesis.

Bibliography

[1] J. Baumgartl, M. Mazilu, and K. Dholakia. Optically mediated particle clearing using airy wavepackets. *Nature photonics*, 2(11):675, 2008.

[2] D.B Ruffner and D.G Grier. Optical conveyors: a class of active tractor beams. *Physical review letters*, 109(16):163903, 2012.

[3] T. Vettenburg, H.I.C Dalgarno, J. Nylk, C. Coll-Lladó, D.E.K Ferrier, T. Čižmár, F.J Gunn-Moore, and K. Dholakia. Light-sheet microscopy using an airy beam. *Nature methods*, 11(5):541, 2014.

[4] N.B Simpson, L. Allen, and M.J Padgett. Optical tweezers and optical spanners with laguerre–gaussian modes. *Journal of modern optics*, 43(12):2485–2491, 1996.

[5] A.K Glaser, Y. Chen, and J.T.C Liu. Fractal propagation method enables realistic optical microscopy simulations in biological tissues. *Optica*, 3(8):861–869, 2016.

[6] A. Elmaklizi, D. Reitzle, A.R Brandes, and A. Kienle. Penetration depth of focused beams in highly scattering media investigated with a numerical solution of maxwells equations in two dimensions. *Journal of biomedical optics*, 20(6):065007, 2015.

[7] J. Van Roey, J. Van der Donk, and P.E Lagasse. Beam-propagation method: analysis and assessment. *Josa*, 71(7):803–810, 1981.

[8] B.H Hokr, J.N Bixler, G. Elpers, B. Zollars, R.J Thomas, V.V Yakovlev, and M.O Scully. Modeling focusing gaussian beams in a turbid medium with monte carlo simulations. *Optics express*, 23(7):8699–8705, 2015.

[9] J. Arnaud. Representation of gaussian beams by complex rays. *Applied optics*, 24(4):538–543, 1985.

[10] J.E Harvey, R.G Irvin, and R.N Pfisterer. Modeling physical optics phenomena by complex ray tracing. *Optical Engineering*, 54(3):035105, 2015.

[11] N.G Worku, R. Hambach, and H. Gross. Decomposition of a field with smooth wavefront into a set of gaussian beams with non-zero curvatures. *JOSA A*, 35(7):1091–1102, 2018.

[12] F. Cai and S. He. Electric field monte carlo simulation of focused stimulated emission depletion beam, radially and azimuthally polarized beams for in vivo deep bioimaging. *Journal of biomedical optics*, 19(1):011022, 2014.

[13] F.A Volpe, P-D. Létourneau, and A. Zhao. Huygens–fresnel wavefront tracing. *Computer Physics Communications*, 212:123–131, 2017.

[14] C. Mignon, A.H. Rodriguez, J.A Palero, B. Varghese, and M. Jurna. Fractional laser photothermolysis using bessel beams. *Biomedical optics express*, 7(12):4974–4981, 2016.

[15] S. Peter, P. Modregger, M.K Fix, W. Volken, D. Frei, P. Manser, and M. Stampanoni. Combining monte carlo methods with coherent wave optics for the simulation of phasesensitive x-ray imaging. *Journal of synchrotron radiation*, 21(3):613–622, 2014.

[16] J.R Mahan, N.Q Vinh, V.X Ho, and N.B Munir. Monte carlo ray-trace diffraction based on the huygens–fresnel principle. *Applied optics*, 57(18):D56–D62, 2018.

[17] M. Mout, M. Wick, F. Bociort, J. Petschulat, and P. Urbach. Simulating multiple diffraction in imaging systems using a path integration method. *Applied optics*, 55(14):3847–3853, 2016.

[18] D.G Fischer, S.A Prahl, and D.D Duncan. Monte carlo modeling of spatial coherence: free-space diffraction. *JOSA A*, 25(10):2571–2581, 2008.

[19] C. Huygens. *Treatise on light*. tredition, 2012.

[20] E. Hecht. *Optics*. Pearson Education, Incorporated, 2017.

[21] C. Huygens, T. Young, A.J. Fresnel, and F. Arago. *The wave theory of light: memoirs of Huygens, Young and Fresnel*, volume 15. American Book Company, 1900.

[22] A. Fresnel. Mémoire sur la diffraction de la lumière. *da p. 339 a p. 475: 1 tav. ft; AQ 210*, page 339, 1819.

[23] G. Kirchhoff. Ann. d. physik. *(2)*, 18:663, 1883.

[24] M. Born, E. Wolf, and A.B. Bhatia. *Principles of Optics: Electromagnetic Theory of Propagation, Interference and Diffraction of Light*. Cambridge University Press, 2000.

[25] J.W. Goodman. *Introduction to Fourier Optics*. W. H. Freeman, 2017.

[26] P.W. Milonni and J.H. Eberly. *Laser Physics*. Wiley, 2010.

[27] Thorlabs Inc. UV fused silica plano-convex lenses. https://www.thorlabs.com/thorproduct.cfm?partnumber=LA4249, 2019. [Online; accessed 18-April-2019].

[28] J.M. Durnin, J.J. Miceli Jr, and J.H. Eberly. Diffraction-free beams. *Physical review letters*, 58(15):1499, 1987.

[29] J.M. Durnin. Exact solutions for nondiffracting beams. I. the scalar theory. *JOSA A*, 4(4):651–654, 1987.

[30] D. McGloin and K. Dholakia. Bessel beams: diffraction in a new light. *Contemporary Physics*, 46(1):15–28, 2005.

[31] D. DeBeer, S.R Hartmann, and R. Friedberg. Comment on" diffraction-free beams". *Physical review letters*, 59(22):2611, 1987.

[32] J.E Harvey and J.L Forgham. The spot of arago: new relevance for an old phenomenon. *American journal of Physics*, 52(3):243–247, 1984.

[33] J. Durnin, J.J Miceli, and J.H Eberly. Reply to d. debeer, sr hartmann and r. friedberg. *Phys. Rev. Lett*, 59:2612, 1987.

[34] P. Sprangle and B. Hafizi. Comment on nondiffracting beams. *Physical review letters*, 66(6):837, 1991.

[35] J. Durnin, J.J Miceli Jr, and J.H Eberly. Durnin, miceli, and eberly reply. *Physical review letters*, 66(6):838, 1991.

[36] Tomáš ČIŽMÁR. *Optické pasti generované netradičními svazky*. PhD thesis, Masarykova univerzita, Přírodovědecká fakulta, 2006.

[37] F. Merola, S. Coppola, V. Vespini, S. Grilli, and P. Ferraro. Characterization of bessel beams generated by polymeric microaxicons. *Measurement Science and Technology*, 23(6):065204, 2012.

[38] B. Aernouts, E. Zamora-Rojas, R. Van Beers, R. Watté, L. Wang, M. Tsuta, J. Lammertyn, and W. Saeys. Supercontinuum laser based optical characterization of intralipid® phantoms in the 500-2250 nm range. *Optics express*, 21(26):32450–32467, 2013.

[39] M.Z. Vardaki, B. Gardner, N. Stone, and P. Matousek. Studying the distribution of deep raman spectroscopy signals using liquid tissue phantoms with varying optical properties. *Analyst*, 140(15):5112–5119, 2015.

[40] P. Di Ninni, F. Martelli, and G. Zaccanti. Effect of dependent scattering on the optical properties of intralipid tissue phantoms. *Biomedical optics express*, 2(8):2265–2278, 2011.

[41] R. Michels, F. Foschum, and A. Kienle. Optical properties of fat emulsions. *Optics Express*, 16(8):5907–5925, 2008.

[42] V. Garcés-Chávez, K. Volke-Sepulveda, S. Chávez-Cerda, W. Sibbett, and K. Dholakia. Transfer of orbital angular momentum to an optically trapped low-index particle. *Physical Review A*, 66(6):063402, 2002.

[43] V. Garcés-Chávez, D. McGloin, M.J Padgett, W. Dultz, H. Schmitzer, and K. Dholakia. Observation of the transfer of the local angular momentum density of a multiringed light beam to an optically trapped particle. *Physical review letters*, 91(9):093602, 2003.

[44] X. Wei, C. Liu, L. Niu, Z. Zhang, K. Wang, Z. Yang, and J. Liu. Generation of arbitrary order bessel beams via 3d printed axicons at the terahertz frequency range. *Applied optics*, 54(36):10641–10649, 2015.

[45] S.N. Khonina, V.V. Kotlyar, V.A. Soifer, M.V. Shinkaryev, and G.V. Uspleniev. Trochoson. *Optics Communications*, 91(3-4):158–162, 1992.

[46] V.V. Kotlyar, A.A. Kovalev, S.N. Khonina, R.V. Skidanov, V.A. Soifer, H. Elfstrom, N. Tossavainen, and J. Turunen. Diffraction of conic and gaussian beams by a spiral phase plate. *Applied optics*, 45(12):2656–2665, 2006.

[47] S. Topuzoski and L. Janicijevic. Conversion of high-order laguerre–gaussian beams into bessel beams of increased, reduced or zeroth order by use of a helical axicon. *Optics Communications*, 282(17):3426–3432, 2009.

[48] S. Qiong-Ge, Z. Ke-Ya, F. Guang-Yu, L. Zheng-Jun, and L. Shu-Tian. Generalization and propagation of spiraling bessel beams with a helical axicon. *Chinese Physics B*, 21(1):014208, 2012.